Received: 5 July 2023 | Revised: 7 October 2023 | Accepted: 20 October 2023

DOI: 10.1002/prep.202300175

Propellants, Explosives, Pyrotechnics

RESEARCH ARTICLE

Pressure-assisted binder jetting for additive manufacturing of mock energetic composites

Levi Kirby[1] | **H. S. Udaykumar**[2] | **Xuan Song**[1,2]

[1]Department of Industrial and Systems Engineering, The University of Iowa, Iowa City, IA, USA

[2]Department of Mechanical Engineering, The University of Iowa, Iowa City, IA, USA

Correspondence
Xuan Song, Department of Industrial and Systems Engineering, The University of Iowa, Iowa City, IA, USA, 52242.
Email: xuan-song@uiowa.edu

Funding information
U.S. Air Force Office of Scientific Research, Grant/Award Number: FA9550-20-1-0700; U.S. National Science Foundation, Grant/Award Number: 2118393

Abstract

Additive manufacturing (AM) has emerged as a promising approach to achieve energetic materials (EMs) with intricate geometries and controlled microstructures, which are crucial for safety and performance optimization. However, current AM methods still face limitations such as limited densities and inadequate solids loading. To overcome these limitations, we have developed a pressure-assisted binder jet (PBJ) process that has the potential to allow for the fabrication of intricate EMs while preserving their desired properties. This study aims to investigate the effects of printing parameters on the microstructures and properties of EMs, including density, solids loading, mechanical properties, and heterogeneity. Our results demonstrate that the PBJ process achieves exceptional properties in EMs, including densities up to 83.4% and solids loading up to 95.4%, surpassing those achieved by existing AM processes. Furthermore, the mechanical properties of the fabricated EMs are comparable to those achieved using conventional fabrication techniques, including a compressive strength of 3.32 MPa, a Young's modulus of 16.68 MPa, a Poisson's ratio of 0.45, a shear modulus of 5.73 MPa, and a bulk modulus of 21.01 GPa. Various test cases were printed to showcase the ability of the PBJ process to create EMs with complex structures and exceptional properties. Micro-computed tomography was employed to analyze the influence of printing parameters on the internal composition and microstructures of the printed specimens.

KEYWORDS
additive manufacturing, density, microstructure, polymer-bonded energetic materials, solids loading

1 | INTRODUCTION

Heterogenous/composite energetic materials (EMs) are a polymer-bonded composite comprised of energetic crystals in a polymer binder matrix. These materials have extensive applications in propellant systems and explosive charges. Traditionally, EMs have been fabricated using cast-curing and press-loading techniques [1–5], which offer simple geometries and relatively uniform compositions. However, recent advancements in additive manufacturing (AM) have demonstrated the capability to fabricate EMs with complex structures and grain gradients, which are not accessible using traditional methods.

Additive manufacturing techniques, including stereolithography, direct ink writing, and fused deposition modeling [6–9] present new possibilities for EM manufacturing [7, 10–13]. The ability to control geometric features and grain gradients allows for customization of run distance, shock propagation, and shock-to-detonation transition rates [14], enabling unique detonation and other energetic performance effects [15–18]. Nevertheless, current AM technologies for EMs face limitations in achieving sufficient density, solids loading, and mechanical properties, when compared to traditional methods [19]. These characteristics are critical for the performance and safety aspects of EMs. Specifically, higher packing density contributes to increased energy and accelerated velocity of detonation [20]; optimized solids loading ensures an appropriate ratio of binder to crystal, facilitating the release of nitrogen-rich gas products necessary for combustion [21]; adequate mechanical properties are essential for maintaining structural integrity under extreme heat and pressure upon detonation of EMs [22–24], while insufficient mechanical properties can pose risks of significant degradation to the safety of EMs [25]. Clearly, there is a need for new AM technologies that can fabricate complex EMs while maintaining desired density, solids loading, and mechanical properties.

This study presents a novel AM process that shows promise in reliably producing complex EMs without compromising density, solids loading, and mechanical properties. The main objective of this paper is to investigate the effects of process parameters on the microstructures and properties of EMs. The structure of this paper is as follows: Section 2 introduces the feedstock materials and the AM process used to fabricate high-performing EMs; this section also presents various characterization methods used to analyze the microstructures and properties of the printed EMs. Section 3 showcases several test cases that feature intricate geometries and presents the effects of key printing parameters such as applied pressure (AP), layer thickness (LT), and step-over (SO) on the density, solids loading, microstructures, and mechanical properties of the printed EMs.

2 | EXPERIMENTAL METHODS

2.1 | Materials

In this study, sucrose was utilized as a mock energetic crystal to ensure safety. This material can mimic the morphology and mechanical behavior of real energetic crystals [26]. Granular sugar was ball-milled for 3 hours and sifted down to a particle size of ~200 μm. Hydroxyl-terminated polybutadiene (HTPB) was chosen as a binder due to the reproducibility, ease of curing, and good mechanical properties which are less dependent on temperature and aging [27]. A HTPB binder solution was prepared using a protocol described in our previous work [28]. The formulation consists of several components, including an HTPB monomer (33.9 wt%, R45M, RCS Inc., Cedar City, UT, USA), a curative (3.7 wt%, isophorone diisocyanate or IPDI from Sigma Aldrich, St. Louis, MO, USA), a tepanol bonding agent (0.6 wt%, HX-752, RCS Inc.), a plasticizer (6.8 wt%, isodecyl pelargonate or IDP, RCS Inc.), and a hexane diluent solvent (55 wt%, Sigma Aldrich).

2.2 | Pressure-assisted binder jetting

To fabricate mock EMs, a modified binder jetting technique named pressure-assisted binder jetting (PBJ) was implemented. Traditional binder jetting processes often face limitations in achieving adequate printing density due to loosely spread powder. To overcome this limitation, a layerwise pressing system was employed in the PBJ process (refer to Figure 1). The pressing system was driven by a motorized lead-screw mechanism (Figure 1d and 1e), and a load cell mounted underneath the powder bed ensured precise control of pressure.

In the fabrication process, a powder spreading system (Figure 1c) was utilized to deliver thin layers of powders. This system consisted of a powder reservoir, a powder bed, and a belt-driven roller. The powder reservoir and powder bed were independently controlled using individual stepper motors and lead screws. The belt-driven roller facilitated the uniform spreading of powder from the powder reservoir to the printing bed. A PipeJet nanodispenser (Biofluidix GmbH, Breisgau, Germany, Figure 1f) was employed to selectively deposit binders. This nanodispenser was mounted on an XY linear stage, enabling precise movement along the X and Y axes. During the printing process, binders were deposited onto the powder bed in a drop-on-demand manner. The deposition took place at a specific interval (e.g., 0.3 mm) determined by the size of the droplets. An optimized interval was selected to enable sufficient overlap between the droplets, ensuring the formation of fully saturated shapes. The automation of the printing system was achieved by Arduino and Qt software.

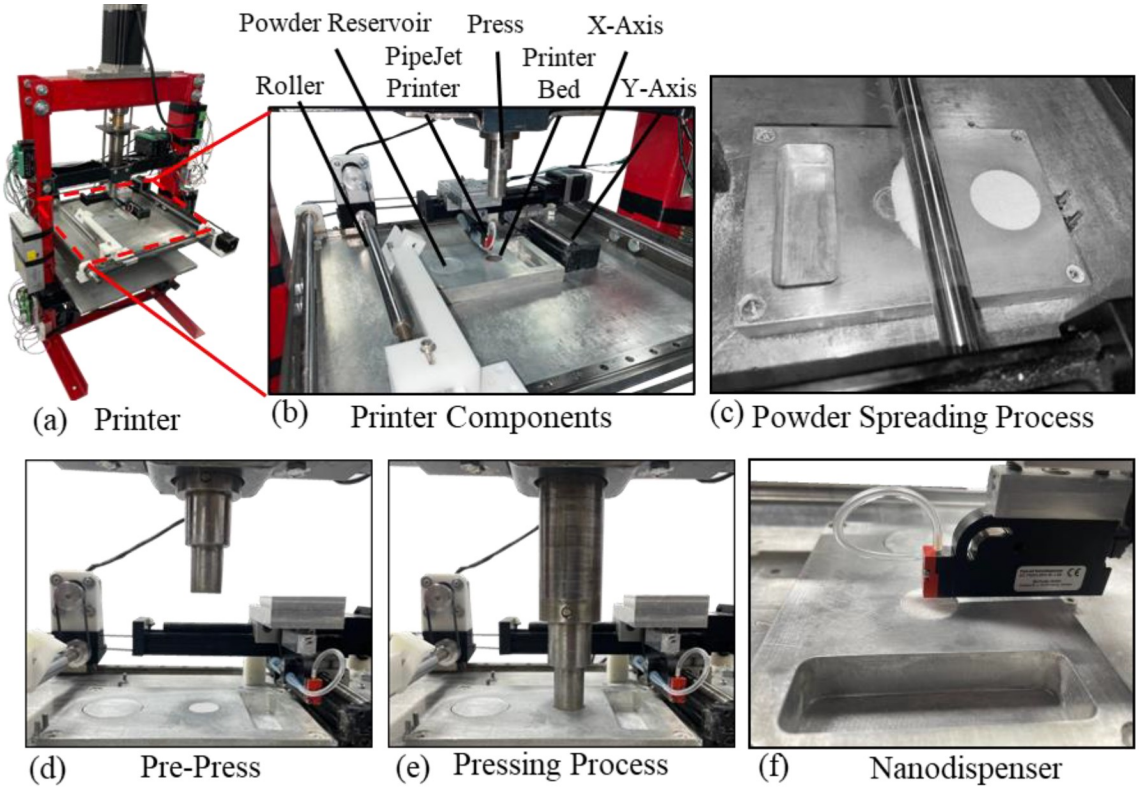

FIGURE 1 (a)(b) The PBJ printing system, (c) the powder spreading system, (d) and (e) the pressing system, and (f) the binder deposition system.

Figure 2 illustrates the step-by-step printing procedures using the PBJ process. The process begins with a computer-aided design (CAD) model, which is sliced using Slic3r software to generate the necessary g-codes for the printer (Figure 2a). When the fabrication of a layer starts, the powder reservoir moves upward while the printer bed moves downward simultaneously (Figure 2b). The roller then transfers a thin layer of powder from the reservoir to the printer bed (Figure 2c). After the powder layer is spread, the press is engaged to compact the powder bed at the desired pressure (Figure 2d). To prevent powder adhesion, Scotch tape was applied to the surface of the press in contact with the powders. Then, the nanodispenser, guided by the predefined tool path in the g-codes, deposits the binder onto the new layer (Figure 2e). These steps repeat until the complete object is fabricated. To cure the binder and evaporate the hexane, the final printed part is heated at 60 °C for one week in an oven (10GCE, Quincy Lab, Inc., Burr Ridge, IL, USA). This curing process is standard for HTPB binder, and tests regarding hexane evaporation is documented in our previous work [28].

2.3 | Printing parameters

This study focuses on investigating three key process parameters that can potentially influence the microstructures and properties of printed EMs. These parameters include applied pressure (AP), layer thickness (LT), and step-over (SO). AP refers to the pressure applied to each layer of powder in the powder bed (Figure 2f). It is an important factor that influences the density and bonding strength of the printed structure. Additionally, AP has an influence on the permeation of the binder into the powder bed. Excessive pressure may lead to extremely low porosity in the compacted powder bed and thereby result in inadequate binder penetration. Our current pressing system is constrained by a maximum pressure of 12 MPa to ensure adequate porosity for effective binder flow. LT is defined as the distance the printer bed moves down for each layer prior to compression (Figure 2g). An appropriate range for LT was identified to ensure binder penetration into the previous layer. SO represents the distance between neighboring toolpaths followed by the nano-dispenser (Figure 2h). A smaller SO

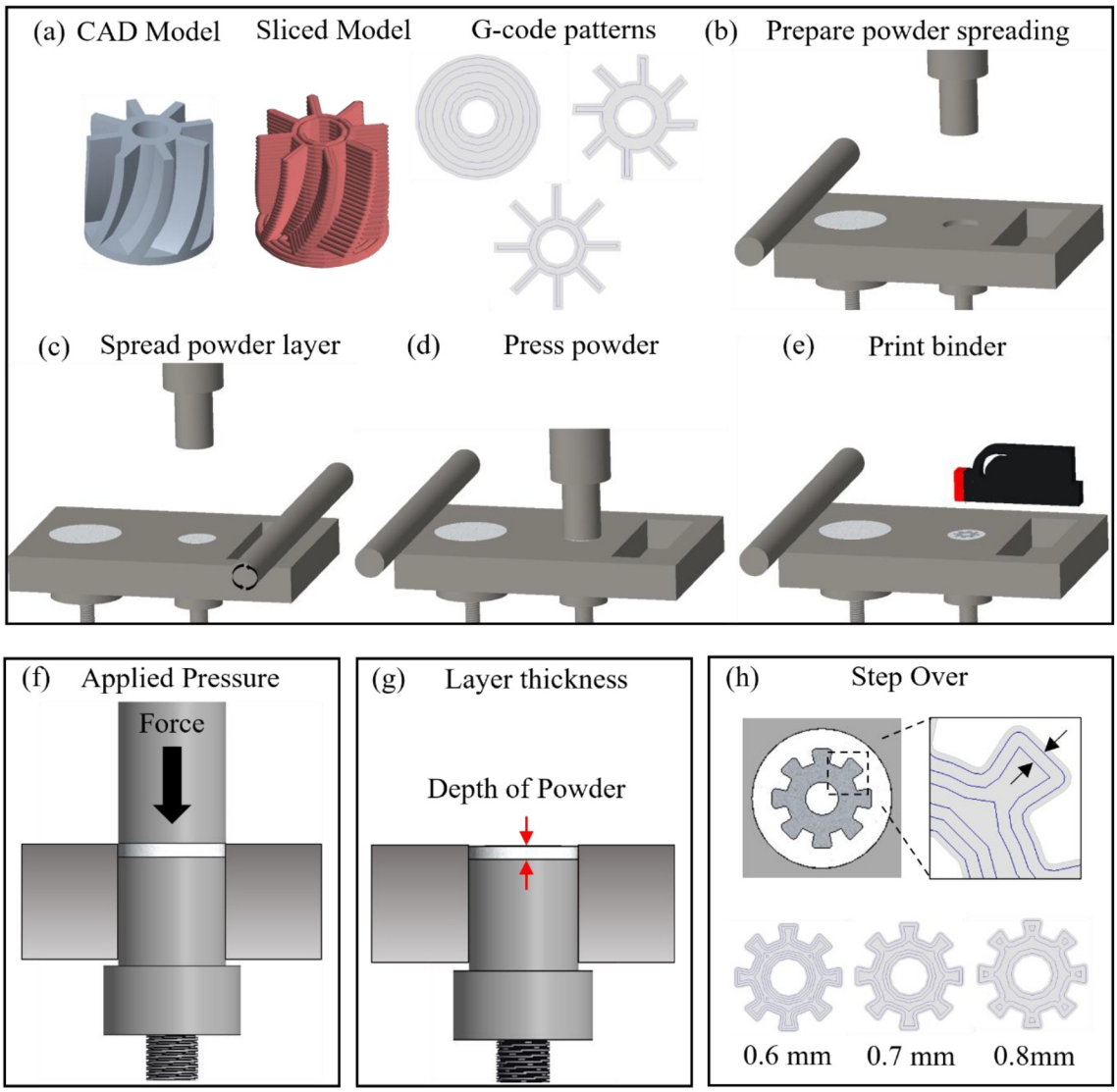

FIGURE 2 (a) PBJ printing process with g-code generation, (b) powder preparing, (c) powder spreading, (d) pressing, and (e) binder deposition. Printing parameters include (f) AP, (g) LT, and (h) SO.

indicates a reduced distance between each pass, leading to a higher amount of binder being deposited per layer.

2.4 | Investigation of solids loading and density

The effects of key process parameters on the solids loading and density of printed mock EMs are experimentally investigated by printing specimens under different combinations of LT (350 μm, 500 μm, and 650 μm), AP (0 MPa, 3 MPa, 6 MPa, and 9 MPa), and SO (0.65 mm, 0.7 mm, 0.8 mm, and 0.89 mm). To determine the solids loading and density of printed mock EMs, a measurement method reported in our previous work [28] was used. The methods are briefly described as follows:

The solids loading of a printed EM was determined using the equation $Solids\,Loading = \frac{m_p}{m_p+m_b} \times 100\,\%$, where m_p is the mass of the sucrose particles in the printed shape, and m_b is the mass of the binder deposited in the printed shape. m_p was estimated using the powder bed density and the volume of the printed shape, V_{print}, while the powder bed density and the volume of the printed shape can be measured using approaches described in the literature [29–32]. m_b was determined from the number of droplets used in the printing and the

droplet volume measured from an integrated optical imaging system.

The density of a printed EM was calculated using the equation $\rho = (VF_p \times \rho_{sucrose}) + (VF_b \times \rho_b)$, where VF_p and VF_b are the volume fraction of the sucrose particles and the binder in the printed shape, respectively, and $\rho_{sucrose}$ and ρ_b are the density of the sucrose particle and the binder, respectively. VF_p was calculated from the powder bed density and the volume of the printed shape V_{print}. VF_b was calculated from the deposited volume of binder and VF_p. The relative density $\rho_{\%}$ was calculated based on the theoretical maximum density (TMD), i.e., the density of a sucrose composite ($\rho_{sucrose} = 0.0016\ g/mm^3$) with pores that are fully saturated with binder.

2.5 | Investigation of mechanical properties

The effects of process parameters on the mechanical properties of printed mock EMs are experimentally investigated through printing specimens under different combinations of AP (0 MPa, 5 MPa, and 10 MPa), LT (350 μm, 500 μm, and 650 μm), and SO (0.6 mm, 0.7 mm, and 0.8 mm). The printed samples had a diameter of 7 mm and a thickness of 5 mm. Seven specimens were printed for each combination of printing parameters. A compression test was performed using a compression machine from TestResources (Shakopee, MN). The compression rate used was 6.35 mm/min. From the loading curve, five mechanical properties were calculated: compression strength, Young's modulus (E), Poisson's ratio (v), shear modulus (G), and bulk modulus (B). The obtained results were compared with those of EMs fabricated using other methods.^

2.6 | Investigation of microstructures

To experimentally investigate the effects of process parameters on the microstructures of printed EMs, specimens were printed under different combinations of AP (0 MPa and 6 MPa), LT (350 μm and 650 μm), and SO (0.6 mm and 0.8 mm). The printed samples had a diameter of 12 mm and a height of 15 mm. The

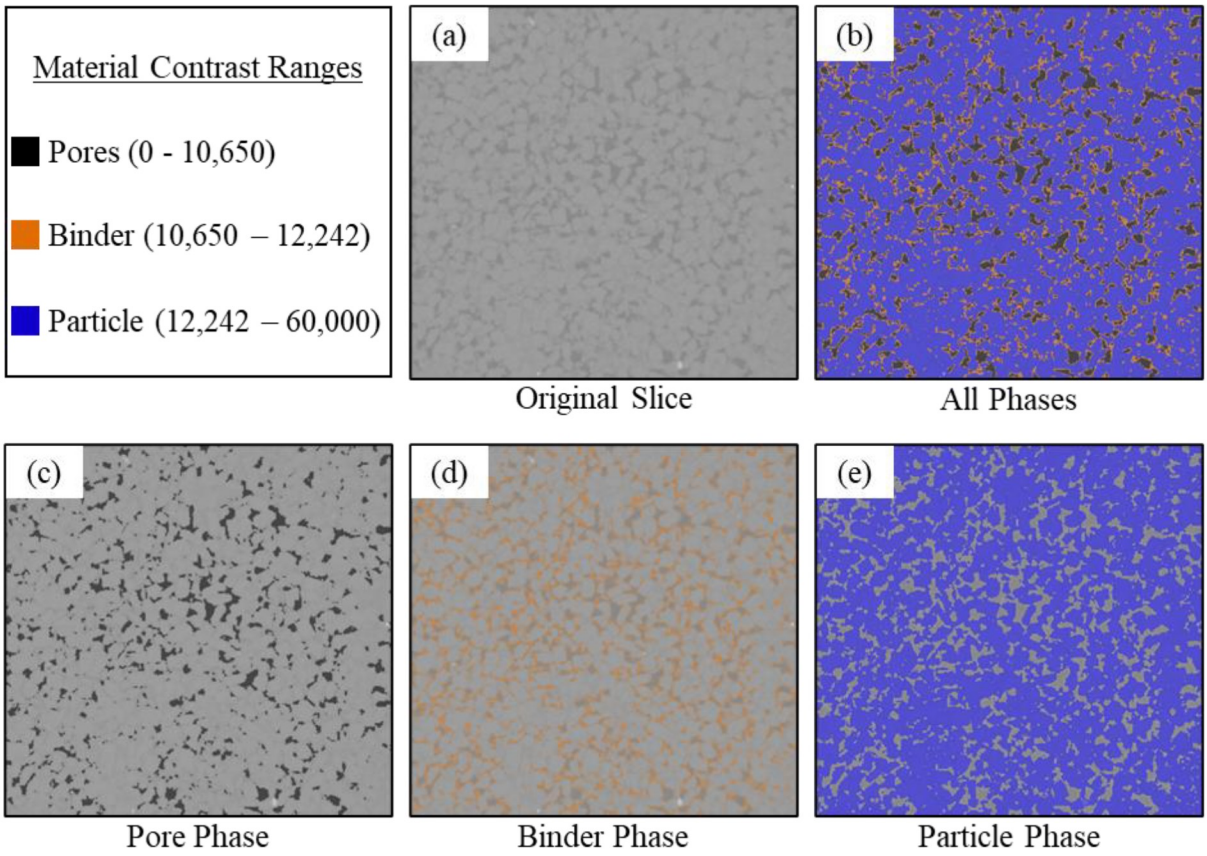

FIGURE 3 Micro-CT images. (a) Original images. Images highlighted with (b) all phases, (c) pores, (d) binder, and (e) particles.

microstructures of the printed specimens were analyzed and quantified using a micro-computed tomography (micro-CT) technique (Zeiss Xradia 520 Versa 3D X-ray microscope). The X-ray source voltage was set to 80 kV with a power of 7 watts. A total of 1601 projections were captured over a 360-degree rotation, with each projection having an exposure time of one second. Image acquisition was performed using a 0.4x objective and an X-ray source-to-sample distance of 43 mm, resulting in a pixel size of 20 μm. Subsequently, the micro-CT scan images were imported into Dragonfly software (Object Research Systems) for further analysis. The software provided tools to differentiate and isolate the sucrose particles, HTPB binder, and pores within each sample by leveraging density contrasts (Figure 3). The contrast range for pores was set at 0–10,650 (Figure 3c). The binder range was found to be 10,650 – 12,242 (Figure 3d), and the sucrose particle had a range of 12,242 – 60,000 (Figure 3e).

2.7 | Statistical analysis

The obtained experimental data were analyzed in statistical software Minitab using Analysis of Variance (ANOVA) to assess significance of the effects of the process parameters on the printed EMs. Before performing the ANOVA, the assumptions of normality, independence, and homogeneity of variances were checked.

3 | RESULTS AND DISCUSSION

3.1 | Test cases

Complex structures were successfully printed to assess the capabilities of the PBJ process in fabricating EMs. Figure 4 shows the successful fabrication results, including a dog model, a multi-port valve, a lattice structure, and a vented gear. The chosen printing parameters were an AP of 10 MPa, a LT of 500 μm, and a SO of 0.7 mm. These printed structures showcase the ability and effectiveness of the PBJ process in producing intricate structures with internal cavities, overhangs, and precise features while maintaining the structural integrity of the samples.

3.2 | Solids loading

The effects of AP and SO on solids loading for different LTs are illustrated in Figure 5a–c. The range of achievable solids loading with these printing parameters falls between 88.3% and 95.4%. The ANOVA test

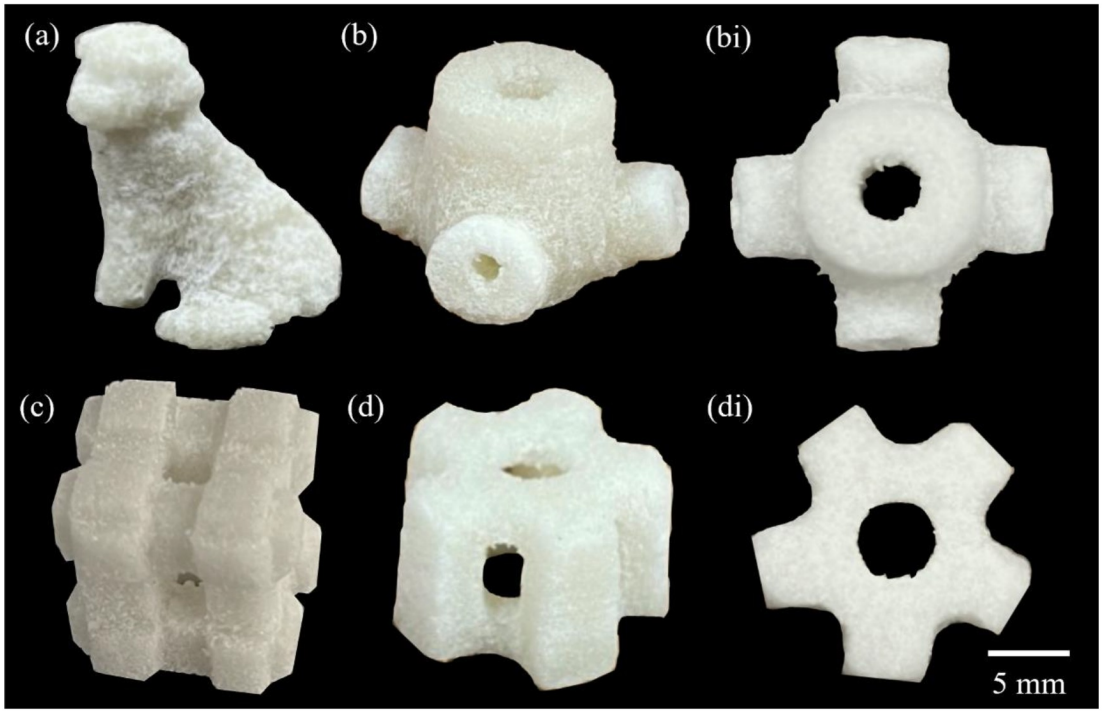

FIGURE 4 Test cases printed by the PBJ process.

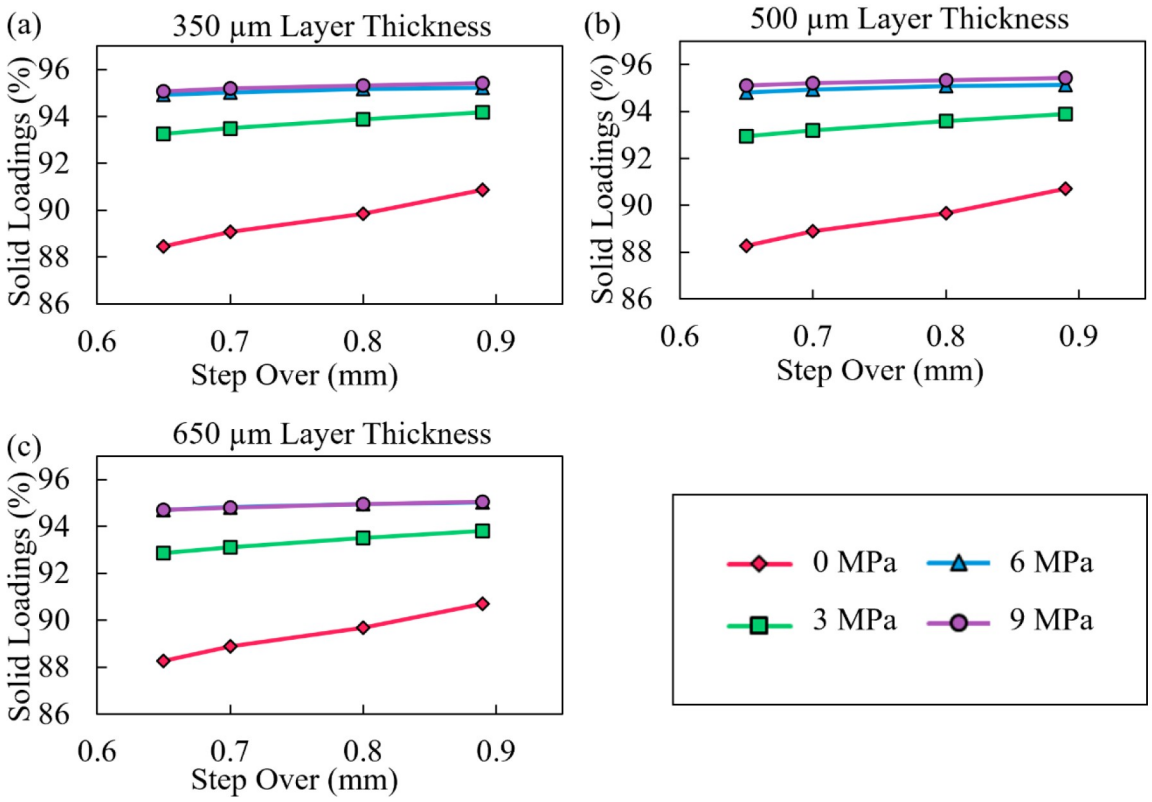

FIGURE 5 The effects of AP and SO on solid loading for different LTs. (a) 350 μm, (b) 500 μm, (c) 650 μm.

reveals that both AP ($p = 0.000$) and SO ($p = 0.000$) have a significant impact on the solids loading, whereas LT shows no obvious effect ($p = 0.1$). Higher APs resulted in higher solids loading by enhancing the powder bed density. The most substantial increase in solids loading occurred when AP increased from 0 MPa to 3 MPa. This is primarily attributed to a substantial reduction in pores within the powder bed during the initial compression stage. Subsequent stages of compression primarily involve particle shifting rather than significant densification, resulting in a relatively smaller influence on the overall solids loading. Increasing the SO also led to an increase in solids loading. A higher SO resulted in a reduced amount of binder being deposited in the sample; consequently, the same quantity of powder received a decreased amount of binder, leading to increased solids loading. The impact of SO on solids loading was more pronounced at lower pressures, as the binder saturation level can be more affected by SO in a more porous powder bed. Based on the results presented in Figure 5, the highest solids loading of 95.4% was achieved when using an AP of 9 MPa, a LT of 500 μm, and a SO of 0.89 mm.

3.3 | Density

The effects of AP and SO on density for different LTs are illustrated in Figure 6a–c. The density attainable with these printing parameters ranges from 63.3% to 83.4%. In comparison to solids loading, density of the printed EMs was more significantly affected by AP ($p = 0.000$) and LT ($p = 0.000$). SO shows negligible effect on the density ($p = 0.14$). The density exhibited a positive correlation with AP, indicating that an increase in AP led to greater reduction in pore size within the powder bed. Similar to solids loading, the most significant change in density occurred between 0 MPa and 3 MPa, due to the substantial reduction of pores during the initial stage of compression. In contrast, an increase in LT led to a decrease in density, which was attributed to an increased level of porosity within the powder bed following the same compaction process. Among the tested parameters, the highest density of 83.4% was achieved when the highest AP, the smallest LT, and the smallest SO were applied.

To evaluate the effectiveness of our process, we compare the achieved density with densities obtained through traditional cast-cure techniques, as illustrated in

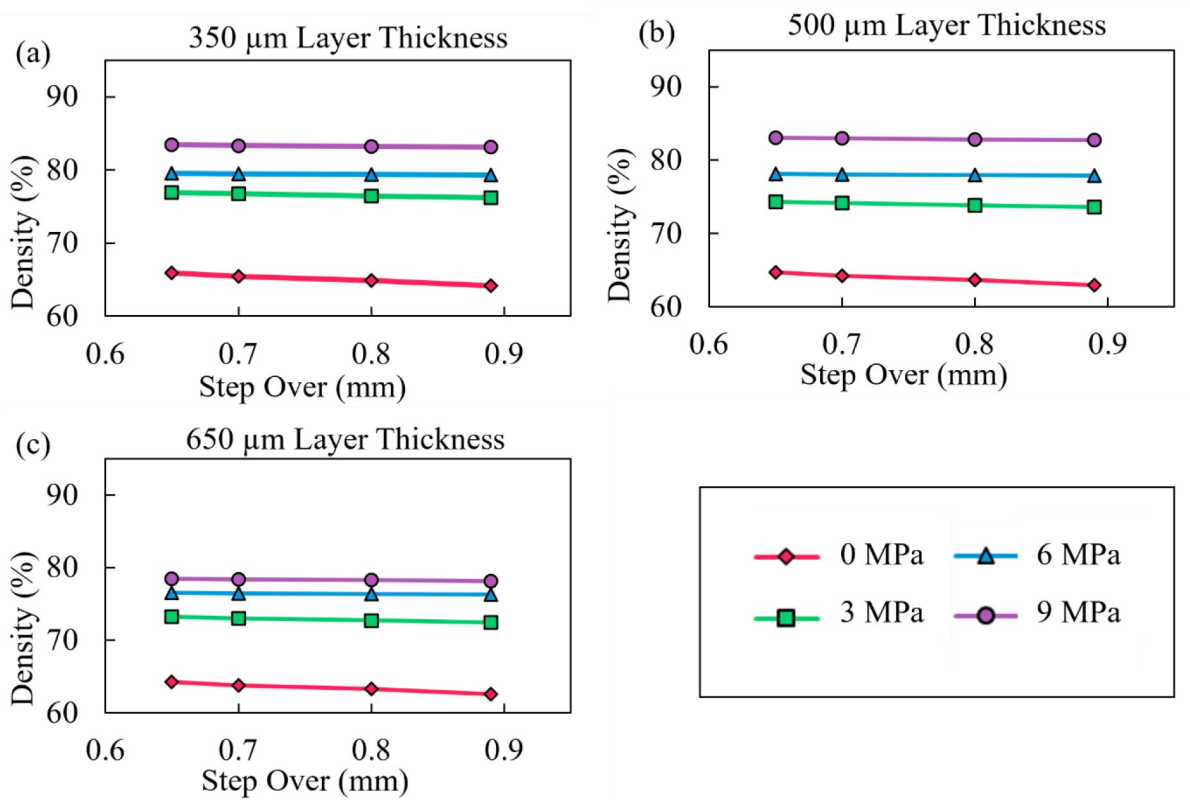

FIGURE 6 The effects of AP and SO on density for different LTs. (a) 350 µm, (b) 500 µm, (c) 650 µm.

Figure 7a. Our PBJ process, at the maximum AP of 12 MPa, yielded a density of 0.00138 g/mm^3. This result is comparable to the density (0.00137–0.00145 g/mm^3) of the cast-cure sample fabricated utilizing a compression of 5.8–90 MPa [33, 34]. It should be noted that the applied compression pressures for some cast-cure samples were 3–7 times greater than in our method. These comparisons highlight the promising results of our method, which could be further enhanced by increasing the pressing capability of our system.

3.4 | Density vs. solids loading

In order to demonstrate the capabilities of our process, a processing map was created that illustrates the correlation between density, solids loading, and various printing parameters, as depicted in Figure 7b. The points on the mapping represent the achieved density and solids loading values for different combinations of SOs, LTs and APs. As the AP changed from 0 MPa to 3 MPa, both density and solids loading underwent the most significant changes. As the AP continued to increase, the differences in density and solids loading become less pronounced.

3.5 | Microstructures

In this section, the effects of different printing parameters on the microstructures of printed EMs are examined using SEM and micro-CT. We analyze the particle density and binder concentrations throughout EMs printed under different printing parameters.

3.5.1 | Applied pressure

The SEM images for samples printed under 0 MPa and 9 MPa are shown in Figure 8a and 8b, respectively. The sample printed under 0 MPa exhibited relatively high porosity, while the sample printed under 9 MPa showed noticeably reduced porosity. Figure 8c presents the reconstructed micro-CT images depicting the effects of different APs (0 MPa, 3 MPa, 6 MPa, and 9 MPa). In these images, the color represents the concentration of particles or binders within the printed samples. The reconstructed images were utilized to quantify the powder packing density, binder concentration, and porosity, as given in Figures 8d–8f.

Figure 8d shows the effect of AP on the powder packing density in printed samples. It is evident that the density was the lowest when no pressure was

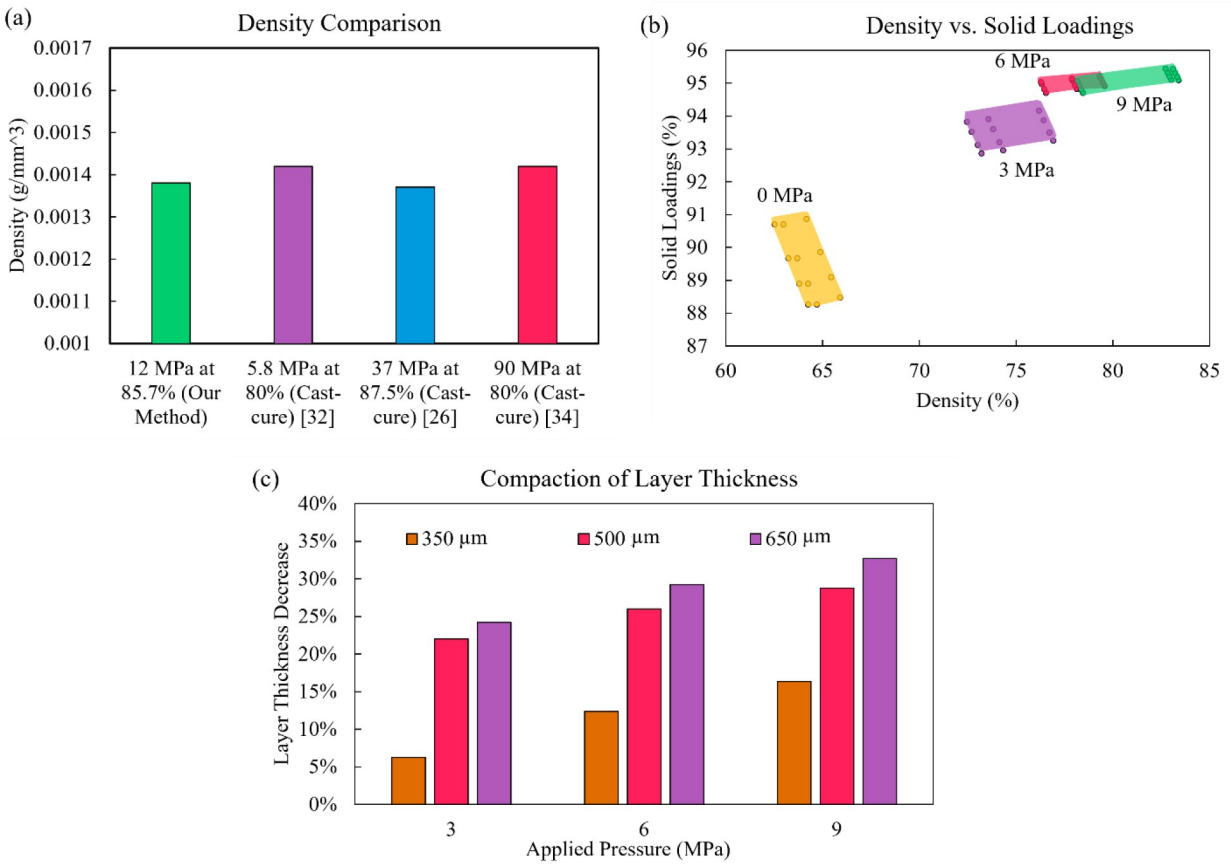

FIGURE 7 (a) comparison of density to other methods; (b) a processing map for density and solids loading; (c) compaction effect on LTs.

applied, and the density remained relatively constant at different heights of the sample. However, when higher pressures (i.e., 3 Mpa–9 MPa) were applied, the powder packing density increased significantly. As the AP increased from 3 MPa to 9 MPa, the packing density showed a more pronounced gradient along the z-direction of the samples. The lower portion of the sample exhibited a higher packing density, because the base powder underwent multiple compression cycles with each subsequent layer.

Figure 8e shows the effect of AP on the binder concentration in printed samples. When the AP was 0 MPa, the binder concentration remained relatively constant at 30%. As the AP increased to 3 MPa, the binder concentration decreased slightly. However, as the AP increased from 3 MPa to 9 MPa, the binder concentration started to increase. This effect can be explained by the interplay between pore reduction and enhanced binder saturation. Pore reduction within the powder bed due to compression leads to a decrease in binder concentration, while enhanced binder saturation contributes to an increase in binder concentration. When AP increases in a low-level range (e.g., 0 Mpa–3 MPa), pore reduction dominates, resulting in a decrease in binder concentration. In contrast, when AP increases in a high-level range (e.g., 3 Mpa–9 MPa), the powder bed becomes denser, and as a result, the kinetics of binder saturation is significantly enhanced, leading to an increase in binder concentration. Furthermore, Figure 8e demonstrates an increase in the gradient of binder concentration as the AP increased. This observation aligns with the trends observed in the powder packing density (Figure 8d).

Figure 8f displayed the final porosity of each sample. It can be observed that the sample printed under 0 MPa exhibited the highest porosity. Despite the higher binder concentration in this sample, the pores were not adequately saturated due to poor powder packing density, resulting in the highest porosity. On the other hand, as the AP increased, the powder packing density improved, allowing for better saturation of pores by the binder. Consequently, samples subjected to higher APs exhibited lower porosity.

Based on the discussion above, it can be concluded that an AP of 3 MPa would be optimal for achieving a balance between density and composition uniformity

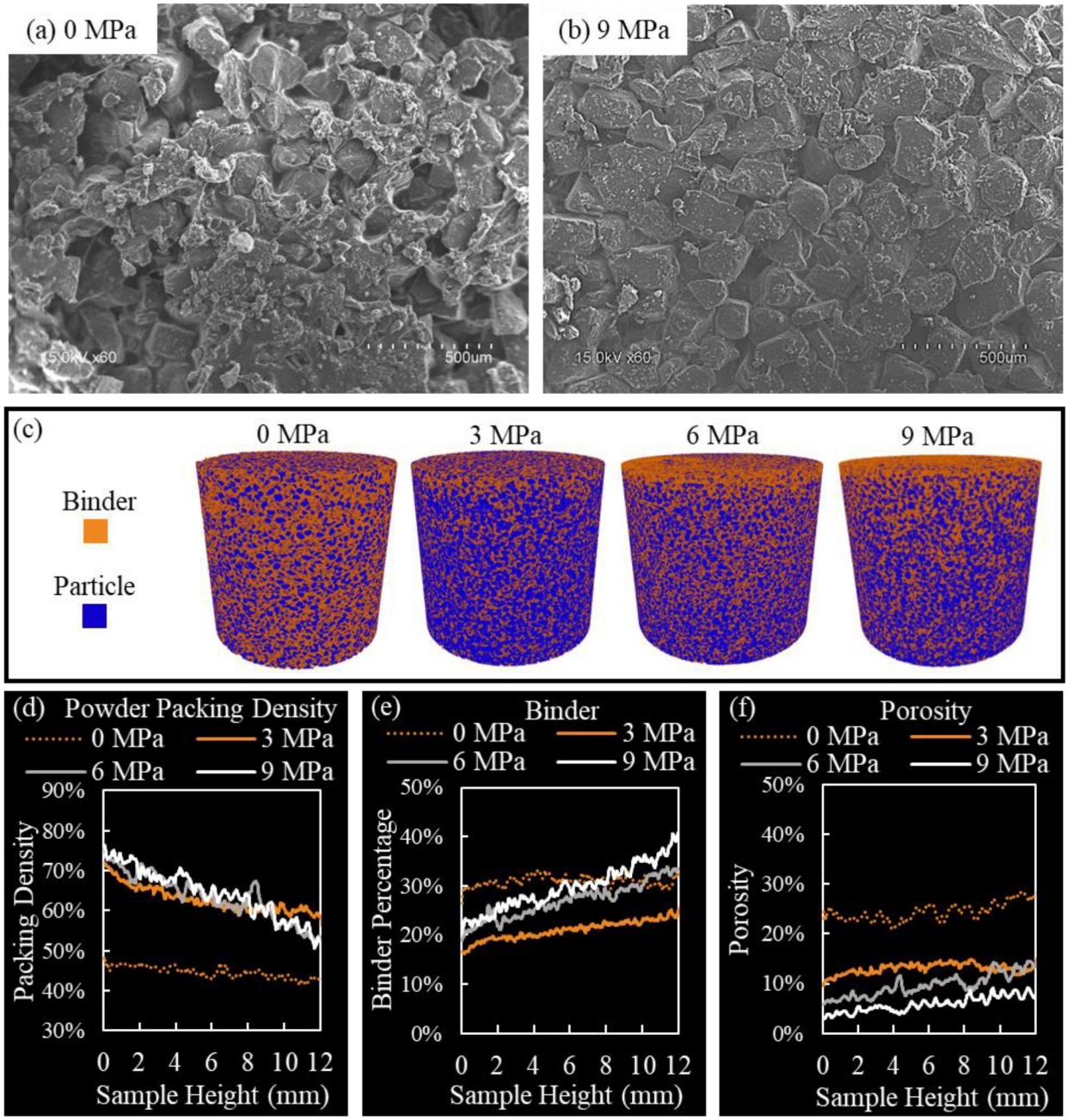

FIGURE 8 Microstructure of samples printed under different APs. (a)(b) The SEM images; (c) the reconstructed micro-CT images; (d) the packing density; (e) the binder concentration; and (f) the porosity.

in printed samples. While the samples printed under 0 MPa demonstrate adequate uniformity, the poor packing density and high porosity compromise their structural strength and overall performance. Conversely, samples printed under a higher AP, such as 9 MPa, exhibit higher powder packing density, sufficient binder concentration, and lower porosity, and have the potential to demonstrate excellent energetic performance if the nonuniformity issues can be addressed in future developments.

3.5.2 | Layer thickness

While previous studies have examined the impact of LT on packing density in binder jetting [35, 36], our study specifically focuses on investigating the effect of LT under layerwise compression. Figure 7c shows how the LT changed when a layer was subjected to different APs. The results indicate that greater LTs were more influenced by compression. For instance, when subjected to an AP of 9 MPa, a layer with a LT of 650 μm experienced

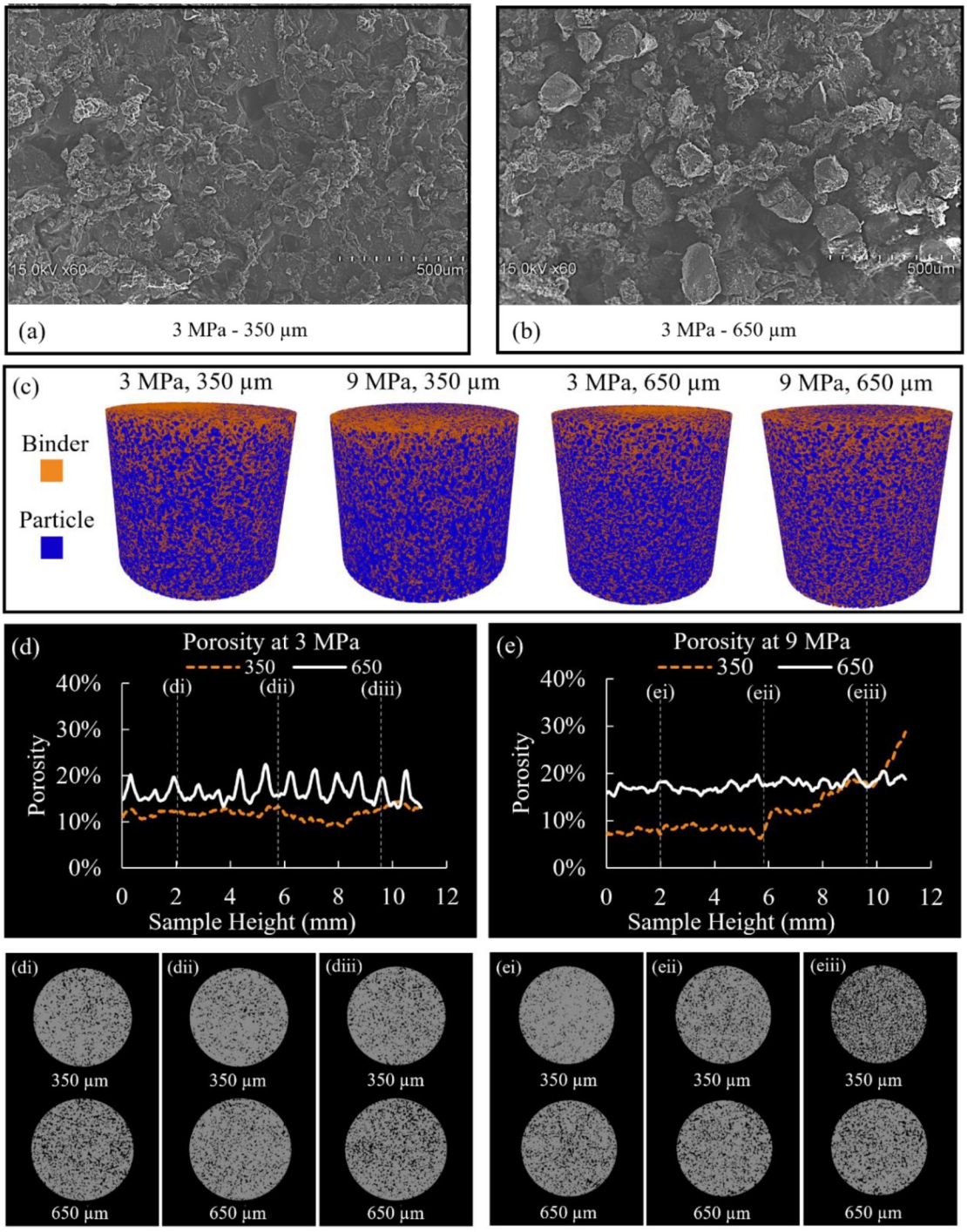

FIGURE 9 Microstructure of samples printed with different LTs. (a)(b) SEM images of different LTs; (c) the reconstructed micro-CT images; (d)(e) the porosity under different pressures; (di–diii) and (ei–eiii) CT sliced images.

a 33% decrease in thickness, while a layer with a LT of 350 μm only exhibited a 16% decrease.

The SEM images in Figure 9a and 9b offer a closer examination of the microstructures formed under different LTs. The images reveal that the lower LT (350 μm) resulted in a more uniform microstructure with improved packing density. In contrast, the sample printed with a LT of 650 μm displayed loose particles and a higher porosity in its microstructure.

Figure 9c presents the reconstructed micro-CT images for samples printed with different LTs. Figure 9d shows the porosity at different heights of samples printed under 3 MPa. For a LT of 350 μm, the porosity was slightly lower and exhibited a more uniform distribution

at the height 0–8 mm. The porosity increased slightly at the height between 8 and 11 mm. The higher porosity at the top can be attributed to the top layers undergoing fewer compression cycles. In contrast, for a LT of 650 μm, the porosity was higher and showed fluctuation along the height. This fluctuation arises from the inability of the binder to fully penetrate the large LT.

Figure 9e depicts the samples printed with different LTs under 9 MPa. Under a LT of 350 μm, the porosity was relatively stable at the height between 0 and 6 mm and exhibited an increasing trend at the height between 6 and 11 mm. Compared to the sample printed with the LT of 350 μm under 3 MPa, the height range with a uniform porosity decreased (0–6 mm vs 0–8 mm). This suggests that when a higher AP is used, a greater number of compression cycles are needed to reach an equilibrium state within a layer. Additionally, it was found that the fluctuation in porosity for the LT of 650 μm was significantly reduced when the higher pressure of 9 MPa was applied. This is because a higher AP reduced the LT to a smaller level, enabling the binder to disperse more evenly throughout the layers and consequently enhancing the uniformity of porosity.

3.5.3 | Step-over

Figure 10 depicts the microstructures and porosity of samples printed using a SO of 0.6 mm and 0.8 mm. Figure 10a shows a surface obtained with a SO of 0.6 mm, which exhibited fewer pores due to effective binder saturation throughout the sample. Figure 10b showcases a more porous surface achieved with a SO of 0.8 mm owing to fewer binder deposited. Figure 10c confirms that the lower SO yielded a slightly lower level of porosity.

3.6 Loading curves

The compression test results in Figure 11 provide valuable insights into the mechanical behavior of the printed samples. Figure 11a displays a sample after yielding during compression. As shown in Figure 11b, the sample subjected to the highest AP exhibited the most significant increase in stress and demonstrated the highest strength. In contrast, the sample subjected to lower AP exhibited a brittle nature and was prone to fracturing. Figure 11c indicates that a smaller LT enabled a higher degree of stress and strain. This can be attributed to the fact that a smaller LT contains fewer pores that need to be eliminated during compression. This, in turn, leads to higher density under the same AP. Additionally, the smaller LT facilitates better diffusion of the binder throughout individual layers, resulting in thorough bonding between all the layers. Conversely, the larger LT received the same amount of binder, which could be insufficient to saturate the entire layer, leading to reduced uniformity and weaker mechanical properties in the resulting parts. Figure 11d suggests SO had little significance in influencing the loading curves, although increasing SO may affect the saturation level in the printed parts.

3.7 | Mechanical properties

Five mechanical properties were calculated from the loading curves, including compressive strength,

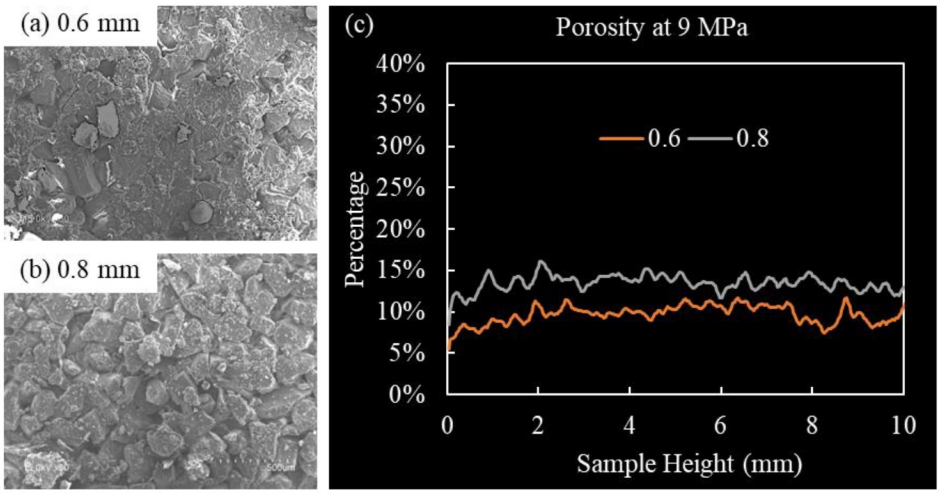

FIGURE 10 Microstructure of samples printed with different SOs. (a)(b) SEM images; (c) Porosity.

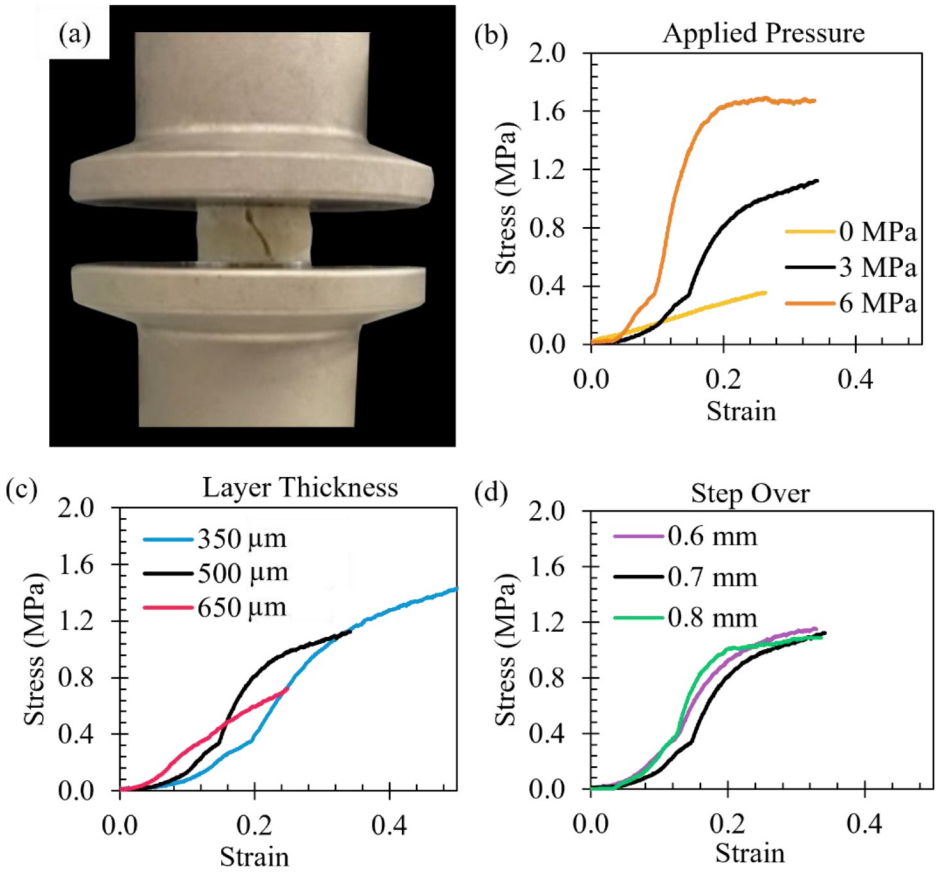

FIGURE 11 Compression test results. (a) The compaction set-up of a specimen. (b)-(d) The stress strain curves.

Young's modulus, Poisson's ratio, shear modulus, and bulk modulus. The results were plotted in Figure 12. Among all the levels of AP, the AP of 6 MPa yielded the highest compressive strength and moduli due to the highest packing density achieved. Among all the levels of LT, the LT of 500 μm led to the highest compressive strength and moduli. The higher LT of 650 μm resulted in excessive pores in the printed sample that could not be fully eliminated by compression, while the lower LT of 350 μm likely contributed to in-process damage to each bonded layer during the compression. The impact of SO on the mechanical properties is negligible. To ensure sufficient mechanical properties in the printed EMs, the selected printing parameters were 6 MPa for AP, 500 μm for LT, and 0.8 mm for SO. Samples were printed using the optimal settings and compared to results obtained from traditional casting methods [1, 37–42]. Figure 13a and 13b reveals our process yielded comparable results to casting methods in terms of Young's modulus and Poisson's ratio. In Figure 13c and 13d, the samples printed by our process exhibited higher bulk modulus and shear modulus than samples obtained through traditional casting methods.

4 | CONCLUSIONS

In this study, we examined the application of a novel PBJ process in fabricating EMs and investigated the influence of three major process parameters, including applied pressure (AP), layer thickness (LT), and step-over (SO), on the quality and properties of printed mock EMs. In comparison with traditional and other AM fabrication methods, our method has the potential to reliably produce complex EMs without compromising density, solids loading, and mechanical properties. Several important findings are summarized as follows:

(1) The PBJ process successfully produced mock EMs with solids loading ranging from 88.3% to 95.4% and densities ranging from 63.3% to 83.4%. These density levels are comparable to traditional cast-cure methods.
(2) The mechanical properties of mock EMs printed through the PBJ process, including compression strength, Young's modulus, Poisson's ratio, shear modulus, and bulk modulus, are comparable to those obtained by many traditional cast-cure processes.

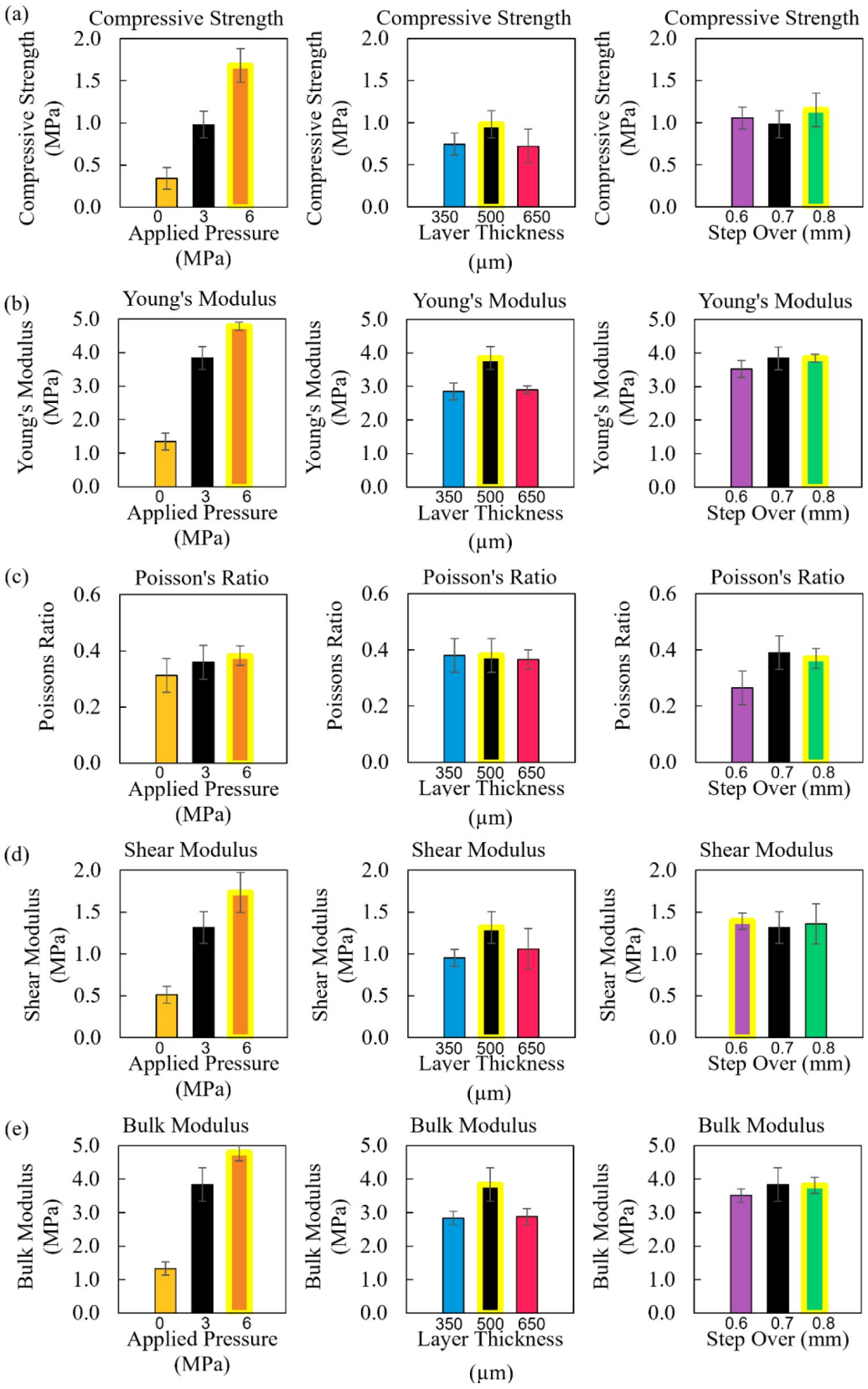

FIGURE 12 Mechanical properties of the printed samples. (a) Compression strength, (b) Young's modulus, (c) Poisson's ratio, (d) shear modulus, and (e) bulk modulus per each set of printing parameters.

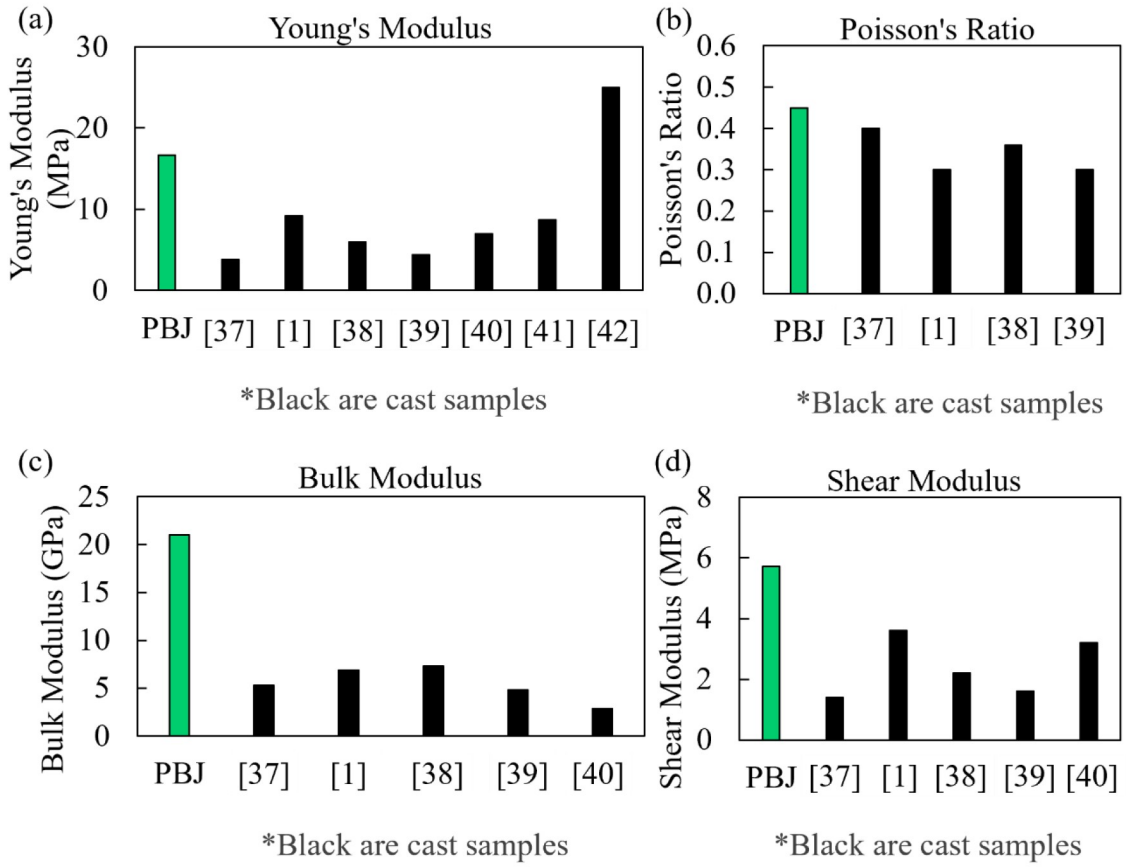

FIGURE 13 Comparison of mechanical properties. (a) Young's modulus, (b) Poisson's ratio, (c) bulk modulus, and (d) shear modulus. The Materials of the compared cast specimens are PBX/HTPB [37], HMX/F [1], TNT/PPESK [38], HMX/HTPB [39], PBX/HTPB [40], AP/HTPB [41], and sugar/PDMS [42].

(3) The AP during the printing process plays a crucial role in determining the microstructures and properties of printed EMs. A higher AP leads to improved powder packing density, enhanced binder saturation, reduced porosity, and thereby better mechanical properties, even though it also results in higher gradients in the powder packing density and binder concentration along the z-direction.

(4) The LT parameter was found to play a crucial role in determining the porosity and uniformity of the printed EMs. Under the same AP, a greater LT tends to achieve a higher porosity with fluctuation along the height, while a smaller LT results in a slightly lower porosity and a relatively uniform porosity within a certain height range. This height range becomes smaller when a higher pressure is applied. Furthermore, suitable LTs need to be selected to ensure consistent and reliable EM performance; a too high LT can contribute to excessive pores in the printed sample that could not be fully eliminated by compression, while a too low LT can result in damage to each bonded layer during compression.

(5) SO has an influence on the solids loading and porosity, in particular when the AP was low, while its influence on the mechanical properties appears to be negligible.

Future research should focus on improved control of the microstructure gradient within the PBJ process. Comprehensive investigations are required to thoroughly explore the process parameter space for achieving diverse microstructure gradients using the PBJ process. Additionally, exploring new formulations of binders for printing EMs using the PBJ process that can reduce the amount of hexane, as the major source for porosity, would further advance the printing quality.

ACKNOWLEDGMENTS

The authors would like to acknowledge the support from the U.S. Air Force Office of Scientific Research under grant number FA9550-20-1-0700 (Program Officer: Martin Schmidt and Chiping Li). H.S.U. and X.S. would also like to acknowledge the support from the U.S. National Science Foundation under grant number 2118393. The

authors thank undergraduate student Thiago Xifra for his help with some of the fabrication.

DATA AVAILABILITY STATEMENT

The data that support the findings of this study are available from the corresponding author upon reasonable request.

ORCID

H. S. Udaykumar http://orcid.org/0000-0002-3655-1483
Xuan Song http://orcid.org/0000-0002-7353-4252

REFERENCES

1. J. Xiao, G. Fang, G. Ji, H. Xiao, *Chin. Sci. Bull.* **2005**, *50*, 21–26.
2. J. R. Carney, J. M. Lightstone, T. P. McGrath, R. J. Lee, *Propellants Explos. Pyrotech.* **2009**, *34*, 331–339.
3. K. Lv, K. Yang, B. Zhou, F. Zhang, J. Guo, C. Han, Y. Tian, *Mater. Des.* **2021**, *207*, 109872.
4. M. Zebregs, A. E. Mayer, A. E. van der Heijden, *Propellants Explos. Pyrotech.* **2020**, *45*, 87–91.
5. M. Szala, *Mater. Wysokoenergetyczne* **2021**, *13*, 5–16.
6. Y. Chen, S. Ba, H. Ren, *Micromachines* **2021**, *12*, 1509.
7. M. Li, W. Yang, M. Xu, R. Hu, L. Zheng, *Mater. Des.* **2021**, *207*, 109891.
8. N. V. Muravyev, K. A. Monogarov, U. Schaller, I. V. Fomenkov, A. N. J. P. Pivkina, *Propellants Explos. Pyrotech.* **2019**, *44*, 941–969.
9. A. K. Murray, W. A. Novotny, T. J. Fleck, I. E. Gunduz, S. F. Son, G. T.-C. Chiu, J. F. Rhoads, *Addit. Manuf.* **2018**, *22*, 69–74.
10. H. Zong, C. Guo, Z. Wang, R. Guo, H. Zhou, G. Hao, H. Ren, L. Xiao, W. Jiang, *J. Energ. Mater.* **2022**, 1–19.
11. H. Woods, A. Boddorff, E. Ewaldz, Z. Adams, M. Ketcham, D. J. Jang, E. Sinner, N. Thadhani, B. Brettmann, *Propellants Explos. Pyrotech.* **2020**, *45*, 26–35.
12. R. Knepper, S. Rupper, S. DeJong, M. P. Marquez, D. E. Kittell, R. L. Schmitt, A. S. Tappan, *J. Appl. Phys.* **2022**, *131*, 155901.
13. C.-G. Song, X.-D. Li, Y. Yang, H.-M. Liu, Y.-X. Tan, J.-Y. Wang, *Def. Technol.* **2021**, *17*, 1936–1943.
14. D. Olsen, M. Zhou, V. Whitley, *Bull. Am. Phys. Soc.* **2022**, 67.
15. Z. Jiba, W. W. Focke, L. Kalombo, M. J. Madito, *Def. Technol.* **2020**, *16*, 316–324.
16. X. Zhou, Y. Mao, D. Zheng, L. Zhong, R. Wang, B. Gao, D. Wang, *J. Mater. Sci.* **2021**, *56*, 9171–9182.
17. N. V. Muravyev, K. A. Monogarov, U. Schaller, I. V. Fomenkov, A. N. Pivkina, *Propellants Explos. Pyrotech.* **2019**, *44*, 941–969.
18. F. D. Ruz-Nuglo, L. J. Groven, *Adv. Eng. Mater.* **2018**, *20*, 1700390.
19. A. Van der Heijden, *Chem. Eng. J.* **2018**, *350*, 939–948.
20. Y. Ma, A. Zhang, C. Zhang, D. Jiang, Y. Zhu, C. Zhang, *Cryst. Growth Des.* **2014**, *14*, 4703–4713.
21. J. Lichthardt, B. C. Tappan, N. De, A. Novak, E. Baca, D. Oschwald, G. Risha, *Propellants Explos. Pyrotech.* **2022**.
22. C. Siviour, M. Gifford, S. Walley, W. Proud, J. Field, *J. Mater. Sci.* **2004**, *39*, 1255–1258.
23. G. Plassart, D. Picart, M. Gratton, A. Frachon, M. Caliez, *Mech. Mater.* **2020**, *150*, 103561.
24. C. Zeng, C. Lin, J. Zhang, J. Liu, G. He, Y. Li, S. Liu, F. Gong, Z. J. C. S. Yang, *Compos. Sci. Technol.* **2019**, *184*, 107842.
25. C. Yu, L. Yang, H. Chen, Y. Qin, T. Wang, W. Sun, C. Wang, *Comput. Mater. Sci.* **2020**, *172*, 109287.
26. E. E. Iglesias, T. Rowe, K. Fernandez, S. Chocron, J. Wilkerson, *J. Compos. Mater.* **2021**, *55*, 2577–2590.
27. H. Naseem, J. Yerra, H. Murthy, P. Ramakrishna, *Energ. Mater. Front.* **2021**, *2*, 111–124.
28. L. Kirby, A. Lawrence, H. S. Udaykumar, T. Sippel, X. Song, *Addit. Manuf.* **2023**, 103808.
29. H. Miyanaji, K. M. Rahman, M. Da, C. B. Williams, *Addit. Manuf.* **2020**, *36*, 101587.
30. H. Miyanaji, N. Momenzadeh, L. Yang, *Addit. Manuf.* **2018**, *20*, 1–10.
31. H. Miyanaji, S. Zhang, L. Yang, *Int. J. Mach. Tools Manuf.* **2018**, *124*, 1–11.
32. W. Du, J. Roa, J. Hong, Y. Liu, Z. Pei, C. Ma, *J. Manuf. Sci. Eng.* **2021**, *143*, 091002.
33. S. Ravindran, A. Tessema, A. Kidane, *Challenges Mech. Time Depend. Mater. Volume 2*, Springer, **2017**, 87–92.
34. S. Ravindran, A. Kidane, *Mech. Compos. Multi-functional Mater. Volume 7*, Springer, **2016**, 345–350.
35. J. Gonzalez, J. Mireles, Y. Lin, R. B. Wicker, *Ceram. Int.* **2016**, *42*, 10559–10564.
36. Z. Xiang, M. Yin, Z. Deng, X. Mei, G. Yin, *J. Manuf. Sci. Eng.* **2016**, *138*, 081002.
37. Y. Q. Xiao, T. Sun, S. S. Li, J. J. Xiao, *J. Phys. Conf. Ser.* **2021**, 012010.
38. Y. Shu, Y. Yi, J. Huo, N. Liu, K. Wang, Y. Lu, X. Wang, Z. Wu, Y. Shu, S. Zhang, *J. Mol. Model.* **2017**, *23*, 1–9.
39. X. J. Wang, J. J. Xiao, *Struct. Chem.* **2017**, *28*, 1645–1651.
40. J. Wang, S. Jin, S. Chen, L. Li, D. Wang, Z. Lu, N. Wang, J. Wang, *J. Mol. Model.* **2018**, *24*, 1–9.
41. M. C. Van Ramshorst, G. L. Di Benedetto, W. Duvalois, A. Hooijmeijer, A. E. van der Heijden, *Propellants Explos. Pyrotech.* **2016**, *41*, 700–708.
42. N. Shirodkar, S. Rocker, G. Seidel, *Smart Mater. Struct.* **2019**, *28*, 104006.

How to cite this article: L. Kirby, H. S. Udaykumar, X. Song, *Propellants, Explos., Pyrotech.* **2024**, *49*, e202300175. https://doi.org/10.1002/prep.202300175